



## Dual cocatalysts decorated CdS nanoparticles for efficient dehydrocoupling of thiols into disulfides

Ming-Hui Sun, Ming-Yu Qi, Zi-Rong Tang <sup>\*,1</sup>, Yi-Jun Xu <sup>\*,1</sup>

College of Chemistry, State Key Laboratory of Photocatalysis on Energy and Environment, Fuzhou University, Fuzhou 350116, PR China



### ARTICLE INFO

**Keywords:**

CdS  
Reduced graphene oxide  
Cobalt phosphate  
Disulfide  
Hydrogen  
Coupling photoredox reaction

### ABSTRACT

Simultaneously utilizing photoinduced electrons and holes to direct splitting of thiols into value-added disulfides and clean hydrogen ( $H_2$ ) fuels conforms the development standards of green chemistry. Herein, a cobalt phosphate (Co-Pi) and reduced graphene oxide (GR) modified CdS photocatalyst is synthesized and utilized for photocatalytic selective conversion of 4-methoxythiophenol (4-MTP) to bis(4-methoxyphenyl) disulfide (4-MPD) coupled with  $H_2$  evolution. In this dual-cocatalyst system, Co-Pi effectively captures and releases the holes from CdS through the chemical state change of Co to accelerate the surface thiols oxidation reaction, while GR is used as an electron collector and an active site for the proton reduction to  $H_2$ . Consequently, the bifunctional GR-CdS-(Co-Pi) photocatalyst demonstrates significantly higher photoactivity than blank CdS. This work affords a new paradigm of incorporating dual-cocatalysts with semiconductor photocatalysts to efficiently take advantage of the photoinduced electrons and holes for photoredox-catalyzed cooperative coupling of organic transformation and  $H_2$  evolution.

### 1. Introduction

Organic disulfides are vital intermediates in the synthesis of biologically and pharmaceutically organic molecules, which have a wide range of applications from antioxidants, drugs, pesticides, to rubber vulcanized reagents [1–4]. From the perspective of synthesis and biology, selective homocoupling of thiols into corresponding disulfides is a valuable chemical procedure. A series of reagents and oxidants have been applied to realize the coupling of thiols in the traditional synthesis strategies, which suffer from long reaction times, poor selectivity and expensive/toxic reagents [5–7]. In this context, selective conversion of thiols or thiophenols to corresponding S–S coupled products *via* photocatalysis provides a sustainable fascinating avenue to obtain high-value disulfides [8]. Most instances of photocatalytic routes require expensive catalysts, generate undesirable overoxidation products and use complex homogeneous catalysts suffering from poor recyclability and catalysts/products separation [9–12]. Some of these catalytic systems cannot simultaneously exploit photoexcited electrons and holes [13–15]. Therefore, there is an urgent and desirable demand to develop a heterogeneous photoredox-based catalytic process, which is highly selective, environmentally benign, less expensive, and sufficiently

utilize the electrons and holes for the cooperative coproduction of clean hydrogen ( $H_2$ ) fuel and value-added disulfides.

Cadmium sulfide (CdS) has garnered significant attention because of its inherent merits, including relatively narrow bandgap optical absorption property and favorable band edge position that satisfy the thermodynamic requirements for many mainstream photocatalytic reactions [16–19]. Nevertheless, owing to the quick recombination of photoinduced charge carriers, photoinstability and the shortage of catalytic active sites, the photoactivity of CdS is still trapped in low conversion efficiency [20,21]. To alleviate this problem, introduction of dual cocatalysts could be a viable way to facilitate the charge separation/transfer, lower the activation energy for redox reactions, and suppress photocorrosion, thereby contributing to an increase in the overall photoredox-catalyzed performance [22,23]. Reduced graphene oxide (GR) has been shown to be an ideal two-dimensional (2D) electronic platform to assemble graphene-semiconductor photocatalysts for enhanced activity [15,24–29]. In addition, cobalt phosphate (Co-Pi) is a kind of notable oxidation cocatalyst for its high abundance and self-healing features [30–33]. Thus, theoretically, if CdS is united with dual cocatalysts of GR and Co-Pi in an appropriate manner, the as-obtained composite photocatalyst would enable sufficient utilization

\* Corresponding authors.

E-mail addresses: [zrtang@fzu.edu.cn](mailto:zrtang@fzu.edu.cn) (Z.-R. Tang), [yjxu@fzu.edu.cn](mailto:yjxu@fzu.edu.cn) (Y.-J. Xu).

<sup>1</sup> Webpage: <http://xugroup.fzu.edu.cn>

of photogenerated electrons and holes for cooperative photoredox reactions.

Herein, we report an efficient GR-CdS-(Co-Pi) ternary photocatalyst for the selective conversion of 4-methoxythiophenol (4-MTP) to bis(4-methoxyphenyl) disulfide (4-MPD) and hydrogen ( $H_2$ ) under mild reaction condition. The optimal ternary GR-CdS-(Co-Pi) composite exhibits significantly enhanced yields of 4-MPD and  $H_2$ , which are approximately 27.3-fold and 6.4-fold as compared to those of blank CdS, respectively, along with an outstanding 4-MPD selectivity of above 99.0 %. The mechanism study validates that the synergistic effect of Co-Pi and GR can significantly facilitate the separation and migration of photo-induced holes and electrons, so that the dehydrocoupling of thiols to disulfides can be carried out efficiently. As indicated by control experiments and electron paramagnetic resonance (EPR) spectra, the photocatalytic dehydrocoupling of thiols proceeds through the process intermediated by sulfur-centered radicals. We hope that this work could provide new guidance for designing cost-effective heterogeneous photocatalysts-based cooperative photoredox systems toward simultaneously utilizing photogenerated electrons and holes for clean energy conversion and valuable organosulfur chemistry.

## 2. Experimental section

### 2.1. Materials

Cadmium acetate dihydrate ( $Cd(CH_3COO)_2 \cdot 2 H_2O$ ), sulfuric acid ( $H_2SO_4$ ), dimethyl sulfoxide ( $C_2H_6OS$ , DMSO), cobalt nitrate ( $Co(NO_3)_2 \cdot 6 H_2O$ ), sodium phosphate monobasic ( $NaH_2PO_4 \cdot 2 H_2O$ ), disodium hydrogen phosphate ( $Na_2HPO_4 \cdot 12 H_2O$ ), hydrochloric acid (HCl), acetone ( $C_3H_6O$ ), potassium permanganate ( $KMnO_4$ ), methyl cyanide (MeCN), hydrogen peroxide 30% ( $H_2O_2$ ), ethanol (EtOH), carbon tetrachloride ( $CCl_4$ ) were supplied by Sinopharm Chemical Reagent Co., Ltd (Shanghai, China). 4-methoxythiophenol ( $C_7H_7OS$ ), 4-methylbenzenethiol ( $C_7H_8S$ ), 4-fluorothiophenol ( $FC_6H_4SH$ ), 4-aminothiophenol ( $C_6H_7NS$ ), 4-ethylbenzenethiol ( $C_8H_{10}S$ ), bis(4-methoxyphenyl) disulfide ( $C_{14}H_{14}O_2S_2$ ), *p*-carboxythiophenol ( $C_7H_6O_2S$ ), thiosalicylic acid ( $C_7H_6O_2S$ ), 4-nitrothiophenol ( $C_6H_4NO_2S$ ), 5, 5-dimethyl-1-pyrroline-N-oxide (DMPO), 4-tert-butylbenzenethiol ( $((CH_3)_3CC_6H_4SH$ ), 4-(trifluoromethyl) benzenethiol ( $C_7H_5F_3S$ ), 4-chlorothiophenol ( $ClC_6H_4SH$ ), tetrabutylammonium tetrafluoroborate ( $((C_4H_9)_4N(BF_4)$ , TBABF<sub>4</sub>, 99%) and triethanolamine (TEOA) were purchased from Aladdin Biochemical Technology Co., Ltd (Shanghai, China). Graphite powder was bought from Qingdao Zhongtian Company, China. The deionized water was acquired from local sources.

### 2.2. Synthesis

#### 2.2.1. Synthesis of graphene oxide (GO)

GO was prepared from natural graphite powder through an improved Hummers method, which includes a strong oxidation procedure in solution [34]. Before using the obtained GO solution, the GO solution was placed in a freeze dryer for 48 h to get fluffy GO solid.

#### 2.2.2. Synthesis of reduced graphene oxide (GR)-CdS composites

GR-CdS composites (x% GR-CdS, x = 1, 3, 5, 7) with different theoretical weight percentage of GO were synthesized through a facile solvothermal procedure, and the GO was reduced to GR during this process. Different amounts of GO powder were evenly dispersed in 80 mL DMSO solution after ultrasonification for 30 min, then 0.3998 g of  $Cd(CH_3COO)_2 \cdot 2H_2O$  was added to the above prepared GO mixture, and continued the ultrasonification for another 30 min. The mixed suspension was put into a 150 mL Teflon-lined autoclave, sealed and maintained at 453 K for 12 h. Thereafter, the target products were gathered by high-speed centrifugation (13,000 rpm, 10 min), washed three times with acetone and two times with ethanol to obtain green solid. The target product was obtained after drying at 333 K. The synthesis process

of blank CdS nanoparticles (NPs) was similar to that of GR-CdS hybrids, except for the addition of GO [35].

#### 2.2.3. Preparation of GR-CdS-(Co-Pi) composites

GR-CdS-(Co-Pi) composites (GR-CdS-x% (Co-Pi), x = 10, 15, 20) with different theoretical weight percentage of Co-Pi were prepared through a facile photodeposition procedure under ambient conditions. Typically, 40 mg of the prepared GR-CdS composite and a certain amount of  $Co(NO_3)_2 \cdot 6H_2O$  were ultrasonicated completely in 0.1 mol sodium phosphate aqueous neutral buffer solution (80 mL). After bubbled in nitrogen ( $N_2$ ) atmosphere for 30 min, the mixture was irradiated with visible light ( $420 nm < \lambda < 780 nm$ ) for 40 min in  $N_2$  atmosphere. The weight percentage of Co-Pi in the GR-CdS-(Co-Pi) hybrids can be varied by adjusting the addition amount of  $Co(NO_3)_2 \cdot 6H_2O$ . The required solid was obtained by suction filtration, thoroughly rinsed with deionized water and then dried in vacuum. The preparation of CdS-15% (Co-Pi) was similar to that of GR-CdS-(Co-Pi) hybrids without the addition of GR. It is worth noting that these obtained samples should be stored in  $N_2$  atmosphere.

### 2.3. Photoactivity testing

The photocatalytic dehydrocoupling of 4-MTP into 4-MPD and  $H_2$  was carried out in a double-walled quartz reactor allocated with a circulating water outer jacket. In a typical process, 5 mg photocatalyst and 50  $\mu$ mol 4-MTP were added into the quartz reactor pre-filled with 5 mL MeCN. The mixture was sonicated for 3 min to get a uniform suspension and bubbled in nitrogen atmosphere for 20 min to purge air before illumination. A 300 W Xe lamp (PLS-SXE 300D, Beijing Perfectlight Co., Ltd.) with an energy output of 264 mW  $cm^{-2}$  as the light source ( $320 nm < \lambda < 780 nm$ ) to trigger the photocatalytic reaction. The reaction condition of control tests or extended tests was similar to that of photocatalytic process. For recycling tests, the used photocatalyst was isolated by centrifugation (13,000 rpm, 5 min) and washed with MeCN, then used for the next activity test. The gases products were quantitatively detected by gas chromatograph (Shimadzu GC-2014 C, MS-5A column, TCD, Ar carrier). And a Nylon syringe filter (0.22  $\mu$ m) was used to filter the suspension to obtain clear solution, which was quantitatively detected by gas chromatography-mass spectrometry (GC-MS, Shimadzu GC-MS-QP 2010 SE, SHRxi-5Sil MS, He carrier).

The conversion of 4-MTP and selectivity of 4-MPD were performed using the following equations [36]:

$$\text{Conversion (\%)} = \frac{n_0 - n_{4-MTP}}{n_0} \times 100$$

$$\text{Selectivity (\%)} = \frac{2 n_{4-MPD}}{n_0 - n_{4-MTP}} \times 100$$

Where  $n_0$  means the amount of 4-MTP that involved in the system initially;  $n_{4-MTP}$  and  $n_{4-MPD}$  respectively indicate the amounts of the residual 4-MTP and the produced 4-MPD after reaction.

The apparent quantum yield (AQY) of 4-MPD for the GR-CdS-(Co-Pi) photocatalyst was performed under a similar reaction condition as that of photocatalytic test, in addition to monochromatic light irradiation at different wavelengths (400, 450, 500, 530 and 600 nm). The photon flux of incident light was estimated by the photoradiometer. The AQY was calculated using this equation [37]:

$$AQY = \frac{N_h}{N_p} \times 100\% = \frac{2 \times N_A \times M \times h \times c}{P \times S \times \lambda \times t} \times 100\%$$

Where  $N_h$  indicates the amount of reaction holes,  $N_p$  indicates the amount of incident photons,  $N_A$  refers to Avogadro constant,  $M$  stands for the molar amount of 4-MPD,  $h$  stands for the Planck constant,  $c$  refers to the speed of light,  $P$  refers to the intensity of the irradiation,  $S$  indicates the irradiation area,  $\lambda$  refers to the wavelength of incident light

and  $t$  stands for the reaction time.

### 3. Result and discussion

#### 3.1. Synthesis and morphology

**Fig. 1a** illustrates the synthetic procedure of cobalt phosphate (Co-Pi) and reduced graphene oxide (GR) co-modified CdS photocatalyst (unless otherwise noted, the following characterizations are mainly focused on 5% GR-CdS-15% (Co-Pi), abbreviated as GR-CdS-(Co-Pi)). Firstly, an improved Hummers method is applied to synthesize graphene oxide (GO) using natural graphite powder as the raw material [34]. As sketched in the atomic force microscopy (AFM) results, the thickness of GO is measured to be approximately 2.2 nm (**Fig. 1b**). Subsequently, the GR-CdS composites are synthesized via growing CdS nanoparticles (NPs) on the platform of GO nanosheets (NSs) through a one-step dimethyl sulfoxide (DMSO) solvothermal method, during which, GO is reduced to be GR [38]. Then GR-CdS binary composite is decorated with amorphous cobalt phosphate (Co-Pi) via a facile photodeposition method. When CdS NPs are illuminated with light in pure  $N_2$  atmosphere,

photoinduced holes can oxidize the  $Co^{2+}$  ions in cobalt nitrate solution to  $Co^{3+}$  ions [31]. Due to the limited solubility in aqueous phosphate buffer mixture with pH= 7 of the  $Co^{3+}$  ions [39], the amorphous cobalt phosphate (Co-Pi) can be *in situ* formed on the surface of CdS NPs where under light irradiation, photoinduced holes could be gathered because Co-Pi is capable of cyclically capturing holes [40].

Scanning electron microscopy (SEM) and transmission electron microscopy (TEM) have been used to obtain the information about the morphology and microscopic structure of the samples. As illustrated in **Fig. S1a** and b, the average diameter of pure CdS NPs is about 200 nm while the prepared GO NSs manifest legible ultrathin two-dimensional (2D) platform, and the SEM images of GR-CdS and GR-CdS-(Co-Pi) composites are displayed in **Fig. S1c** and d. The TEM images in **Fig. 1c** and d exhibit detailed morphology information of GR-CdS-(Co-Pi), the identified edge area of each component in GR-CdS-(Co-Pi) hybrids implies that the tight interfacial interaction between GR NSs, CdS NPs and the Co-Pi layers has been obtained. Distinctively, the particle size of CdS NPs in binary composites decreases from 200 nm to about 10 nm, indicating that the introduced GR NSs can be used as growth platform to prevent the aggregation of CdS NPs [41]. Afterwards, the microstructure

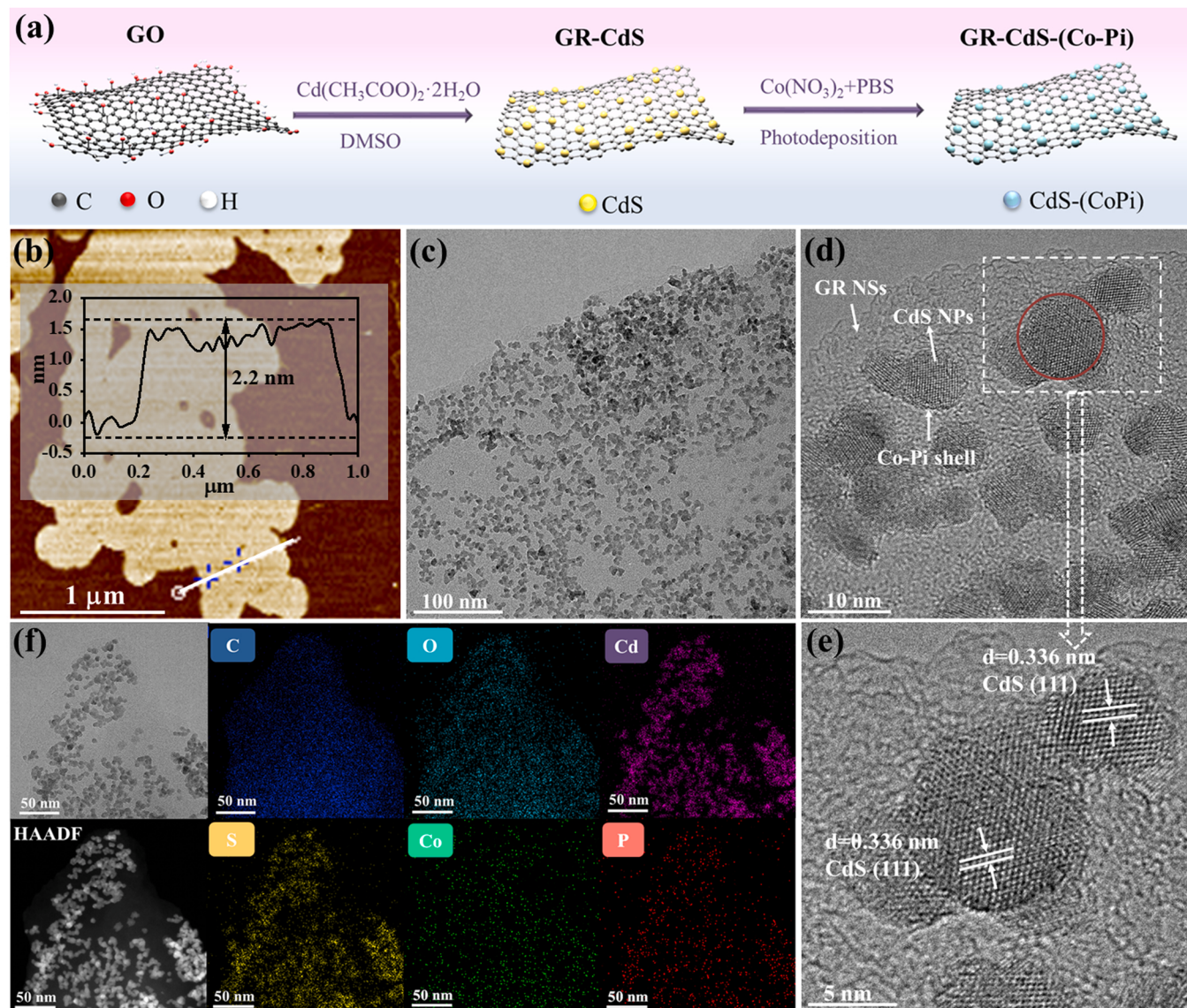


**Fig. 1.** (a) Schematic illustration of the synthesis of GR-CdS-(Co-Pi) composite. (b) Atomic force microscopy (AFM) image of GO. (c, d) TEM images of GR-CdS-(Co-Pi) composite. (e) HRTEM image of GR-CdS-(Co-Pi) composite. (f) The elemental mapping images of GR-CdS-(Co-Pi) composite.

information of GR-CdS-(Co-Pi) composites has been further gained through high-resolution TEM (HRTEM) characterizations. As observed in Fig. 1e, the 0.336 nm lattice fringe corresponds to the (111) facet of cubic CdS [42]. On account of the amorphous nature of Co-Pi, no obvious characteristic lattice spacing can be observed from the Co-Pi shell [32,43,44]. The atomic force microscopy (AFM) results in Fig. S2 suggest that the thickness of ternary GR-CdS-(Co-Pi) composite is about 2.4 nm. To further analyze the elements composition and distribution, element mapping and energy-dispersive X-ray spectroscopy (EDX) have been performed. As demonstrated in Fig. 1f, elements C and O are confined in the large platform of the GR NSs, whereas elements Cd, S, Co and P indexed to CdS and Co-Pi are uniformly dispersed on the whole GR platform. In addition, EDX measurement of the GR-CdS-(Co-Pi) composites has also demonstrated the existence of C, O, Cd, S, Co and P elements (Fig. S3).

### 3.2. Physicochemical properties

To further determine the chemical element compositions of the GR-CdS-(Co-Pi) composite, the X-ray photoelectron spectroscopy (XPS) measurement has been carried out. As sketched in the XPS survey spectra of CdS, GR-CdS and GR-CdS-(Co-Pi) composites (Fig. S4), all elements (Cd, S, C, O, Co and P) corresponding to GR-CdS-(Co-Pi) are shown in Fig. S4c, which further affirm the elemental mapping results. The C 1s and O 1s spectra are displayed in Fig. S5a and b. As exhibited in Fig. S5a, the C 1s spectrum of GR fitted into three peaks can be indexed in detail to diverse functional groups, such as the C—C, C=C & C—H at 284.80 eV, the C—O bond at 286.12 eV and the C=O bond at 288.45 eV [42]. In the Cd 3d spectrum of the ternary GR-CdS-(Co-Pi) composite (Fig. 2a), the two peaks located at 405.98 and 412.73 eV are respectively attributed to Cd 3d<sub>5/2</sub> and Cd 3d<sub>3/2</sub> [45]. For the S 2p XPS spectra, the binding energy of S 2p<sub>3/2</sub> at 162.35 eV together with S 2p<sub>1/2</sub> at 163.57 eV are ascribed to S<sup>2-</sup> in CdS (Fig. 2b) [46]. For the Co 2p spectrum sketched in Fig. 2c, two peaks fixed at 781.50 and 797.30 eV

are assigned to the binding energies of Co 2p<sub>3/2</sub> and Co 2p<sub>1/2</sub>, respectively, demonstrating the existence of Co<sup>3+</sup> and surface-adsorbed Co<sup>2+</sup> ions of the ternary sample, which is in line with Co-Pi species reported in the previous literature works [31,40,47,48]. Fig. 2d shows that the binding energy of P 2p is located at 133.40 eV, confirming that the presence of phosphate group [48]. Noticeably, as depicted in Fig. 2a and b, the characteristic element peaks corresponding to CdS exhibit a significant shift to higher binding energy after the intervention of GR, manifesting that closer interfacial contact and stronger electronic interaction have been formed between CdS and GR [42]. Above results manifest the coexistence of GR and Co-Pi in the GR-CdS-(Co-Pi). X-ray diffraction (XRD) analysis has been used to investigate the crystal structure properties of the different composites. As displayed in Fig. 2e, the peaks of blank CdS situated in 2θ values of ca. 26.86°, 44.18°, and 52.26° can be indexed as (111), (220) and (311) planes of cubic phase CdS (JCPDS No.10-0454) [42]. CdS, GR-CdS and GR-CdS-(Co-Pi) composites show similar XRD patterns to those of pure CdS NPs. The XRD signals of Co-Pi are consistent with those of monoclinic Co<sub>3</sub>(PO<sub>4</sub>)<sub>2</sub>·8 H<sub>2</sub>O (JCPDS NO.33-0432) [49], and the diffraction peak of GR is not observed in these composites, which is owing to the relatively low diffraction intensity of GR [42]. Moreover, the XRD spectra of GR-CdS composites with different percentages of GR (Fig. S6) and GR-CdS-(Co-Pi) composites with different percentages of Co-Pi (Fig. 2e) further certify that the crystallographic structure of CdS NPs is not influenced by the decoration of GR or Co-Pi, and the percentages of dual cocatalysts have no apparent influence on the crystalline phase of the CdS NPs.

Raman spectra are applied to further detect the phase composition of blank GR, blank CdS, GR-CdS and GR-CdS-(Co-Pi) (Fig. 2f). From the Raman spectra, two strong and wide peaks can be observed at 304.53 and 603.35 cm<sup>-1</sup>, which can be indexed to the E<sub>1</sub> and 2E<sub>1</sub> vibrational modes of CdS, respectively [50]. Two adjacent peaks located at 1360.39 and 1601.93 cm<sup>-1</sup> are ascribed to the D band and G band of GR, respectively [51]. Ultraviolet-visible (UV-vis) diffuse reflectance

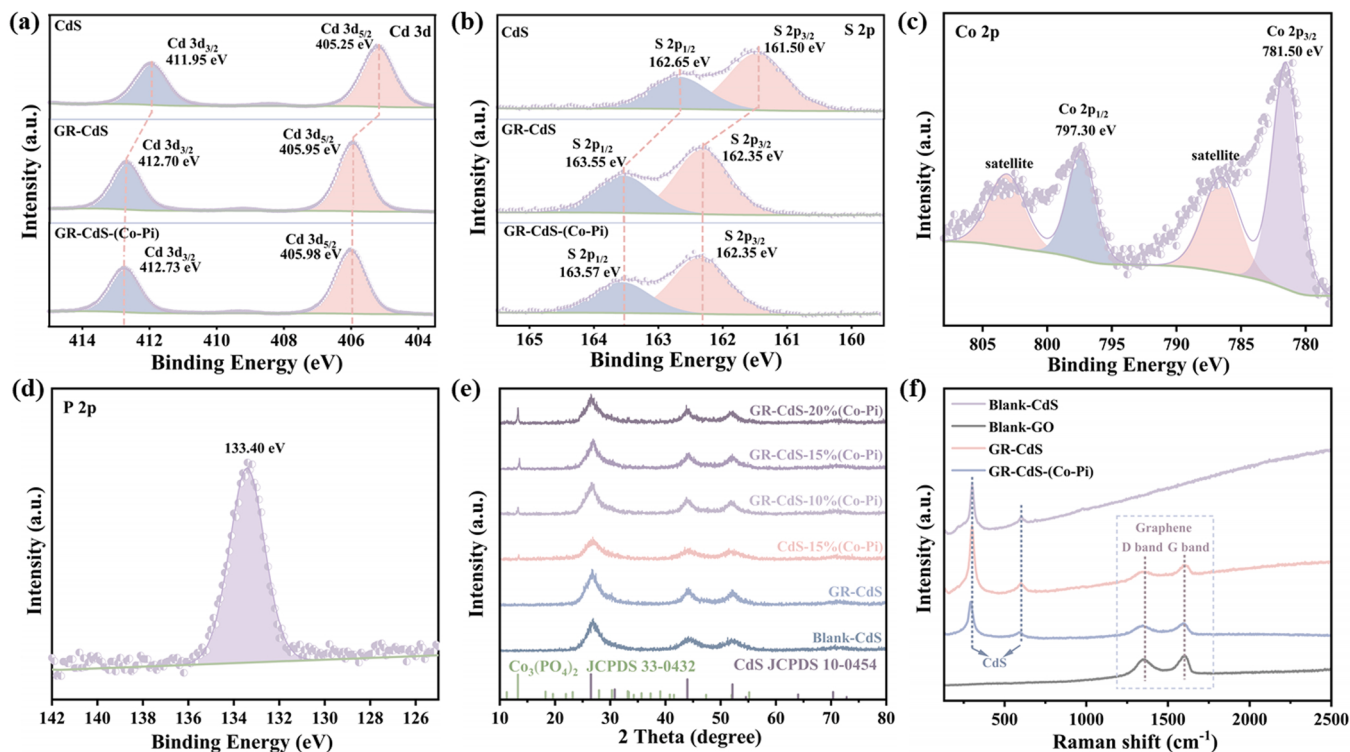


Fig. 2. XPS results of (a) Cd 3d and (b) S 2p of CdS, GR-CdS and GR-CdS-(Co-Pi) composites, (c) Co 2p and (d) P 2p of GR-CdS-(Co-Pi) composite. (e) XRD spectra of blank CdS, GR-CdS, CdS-15% (Co-Pi) and GR-CdS-x% (Co-Pi) ( $x = 10, 15, 20$ ) composites. (f) Raman spectra of blank CdS, blank GO, GR-CdS and GR-CdS-(Co-Pi) composites.

spectra (DRS) have been examined to probe the optical characteristics of the GR-CdS-(Co-Pi) composites. As indicated in Fig. S7, CdS shows the absorption edge of about 520 nm, which is correlated to the intrinsic absorption of CdS [52]. Owing to the forceful absorption of GR and Co-Pi, the absorption intensities of GR-CdS and GR-CdS-(Co-Pi) composites increase gradually in the visible light range (520–760 nm) [44, 53]. The aforementioned results evidently convince the successful synthesis of GR-CdS-(Co-Pi) ternary composite.

### 3.3. Coupling photoredox-catalyzed reaction for cooperative 4-MTP conversion and $H_2$ generation

The photocatalytic performances of blank CdS NPs, GR-CdS and GR-CdS-(Co-Pi) composites have been measured through a photoredox-catalyzed system of dehydrogenative coupling of 4-MTP to 4-MPD pairing with  $H_2$  evolution (Fig. 3a). The GC-MS analysis has been carried out to determine the structure and concentration of different liquid products (Figs. S8 and S9). As plotted in Fig. 3b, the blank CdS presents extremely low activity for  $H_2$  evolution (0.8  $\mu\text{mol}$ ) and 4-MPD generation (3.6  $\mu\text{mol}$ ), and the photoactivities of CdS composites are raised with decoration of the GR cocatalyst (8.0  $\mu\text{mol}$  for  $H_2$  production and 9.4  $\mu\text{mol}$  for 4-MPD yield). After introduction of the Co-Pi cocatalyst, the production efficiencies of 4-MPD and  $H_2$  are significantly increased of GR-CdS-(Co-Pi) ternary composites (Fig. 3c). The GR-CdS-15% (Co-Pi) composite displays the optimal  $H_2$  and 4-MPD productions of 21.0 and

22.8  $\mu\text{mol}$ , respectively, which achieve about 27.3 and 6.4 folds higher than those of the CdS. And the conversion of 4-MTP increases from 15.0 % to 85.2 %. Besides, the liquid product 4-MPD exhibits an excellent selectivity of 99.0 % over 5 h with no evidence of over-oxidation. Notably, excessive decoration of Co-Pi is not conducive to the improvement of photocatalytic activity because of the active reaction sites shielding effect [32]. The apparent quantum yield (AQY) of 4-MPD is affected by the light wavelength under various monochromatic lights illumination and is closely related to the DRS spectrum of GR-CdS-15% (Co-Pi) (Fig. 3d). More importantly, the current catalyst system has further been tested to convert 4-MTP in scale-up reactions (7.1 mmol of substrate 4-MTP, Table S1). As is clearly seen, a 4-MTP conversion of about 92.2 % within 30 h can be obtained, accompanying by a 4-MPD yield and selectivity of 92.0 % and 99.7 %, respectively. In addition, the amount of evolved  $H_2$  reaches the maximal value of 3.1 mmol in 30 h, suggesting a stoichiometric dehydrocoupling reaction. The coproduction of  $H_2$  and 4-MPD in gram scale demonstrates the practicability of this dual-cocatalysts photoredox system for cooperative coupling of organic transformation and  $H_2$  evolution under ambient conditions.

Furthermore, we also extend the photoredox dehydrocoupling of thiophenols to other substituted thiophenols with electron-contributing groups or electron-withdrawing groups, and obtain the corresponding target products in varying degrees of yields and selectivity (Table 1, entries 1–10). To explore the photostability and recyclability of

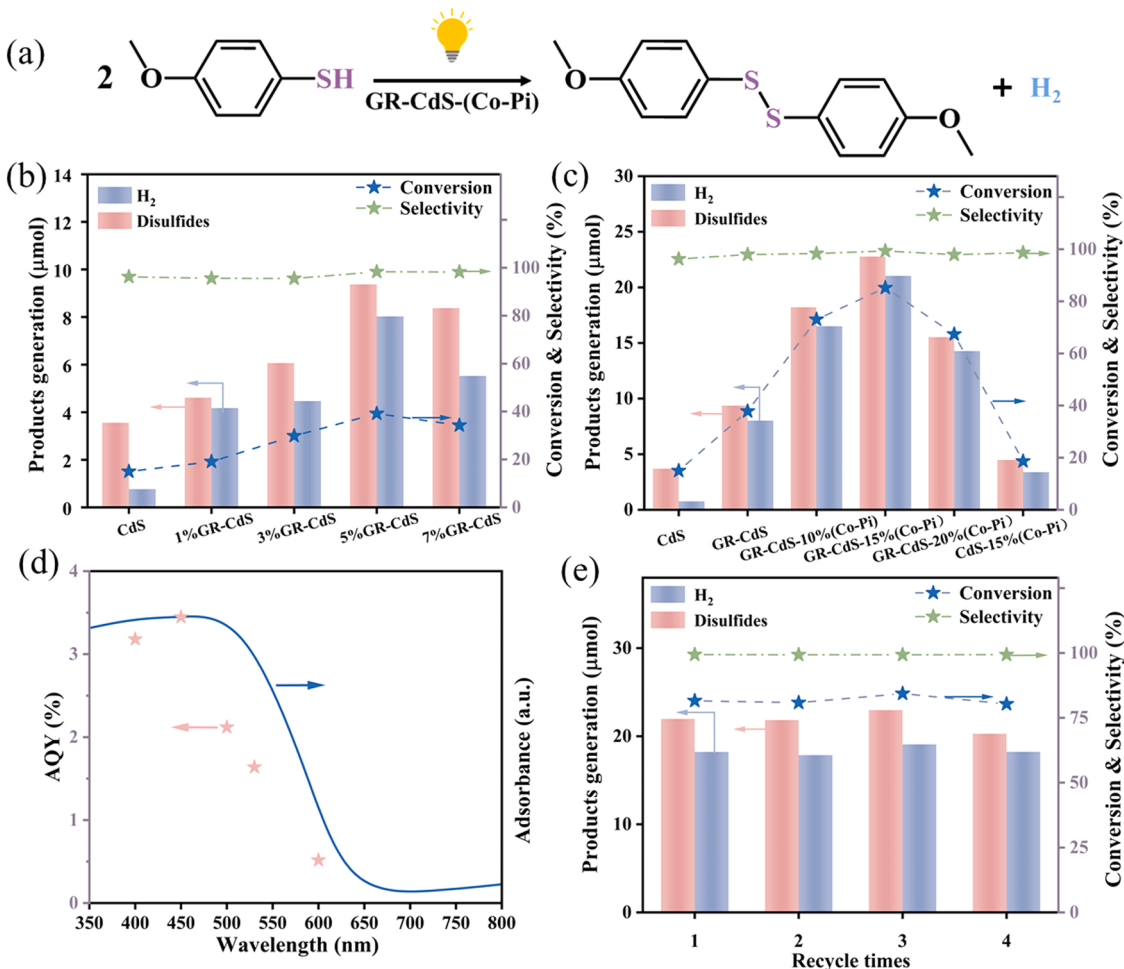


**Fig. 3.** (a) The formula of photocatalytic activity tests of selective thiol oxidation into disulfide integrated with  $H_2$  evolution. (b) Photocatalytic activity of blank CdS,  $x\%$  GR-CdS ( $x = 1, 3, 5, 7$ ). (c) Photocatalytic activity of blank CdS, GR-CdS, GR-CdS- $x\%$  (Co-Pi) ( $x = 10, 15, 20$ ) and CdS-15% (Co-Pi) composites. (d) DRS spectrum of GR-CdS-15% (Co-Pi) composite and AQY of 4-MPD under different wavelengths illumination. (e) Photocatalytic cyclic tests over GR-CdS-15% (Co-Pi) composite. (Reaction conditions of photocatalytic tests and recycling tests: 5 mg catalysts, 50  $\mu\text{mol}$  thiophenol, 5 mL MeCN, full spectrum, irradiation for 5 h.).

**Table 1**Substrate scope for the conversion of thiophenols into disulfides and H<sub>2</sub> production <sup>a</sup>.

Entry	-R	Thiophenol conversion (%) <sup>b</sup>	Thiophenol selectivity (%) <sup>c</sup>	H <sub>2</sub> product (μmol)	e <sup>-</sup> /h <sup>+</sup> <sup>d</sup>
1	-Me	80.4	99.3	17.6	0.88
2	-Et	47.8	98.3	10.5	0.88
3	-CMe <sub>3</sub>	18.7	99.5	4.4	0.95
4	-CF <sub>3</sub>	26.9	99.0	6.6	0.98
5	-F	65.1	99.9	15.5	0.95
6	-Cl	19.2	98.8	4.8	0.99
7	-NH <sub>2</sub>	72.8	97.7	16.0	0.88
8	-NO <sub>2</sub>	61.5	99.3	14.9	0.97
9	p-COOH	ND <sup>e</sup>	trace	trace	0
10	o-COOH	NR <sup>f</sup>	0	0	0

<sup>a</sup> Reaction conditions: 0.05 mmol of thiophenol, 5 mL of MeCN, 5 mg of photocatalyst. The solution was bubbled with Ar for 20 min and was irradiated with 300 W Xe lamp for 5 h at room temperature.

<sup>b</sup> Conversion (%) = [n<sub>0</sub>(thiophenol)-n(thiophenol)]/n<sub>0</sub>(thiophenol) × 100%

<sup>c</sup> Selectivity (%) = 2 n(disulfide)/[n<sub>0</sub>(thiophenol)-n(thiophenol)] × 100%

<sup>d</sup> The ratio of electrons and holes consumed in redox reactions was calculated by the equation of e<sup>-</sup>/h<sup>+</sup> = 2 n(H<sub>2</sub>)/[n<sub>0</sub>(thiophenol)-n(thiophenol)].

<sup>e</sup> Not determined owing to extremely low conversion.

<sup>f</sup> Not reaction.

photocatalyst, cyclic tests over blank CdS (Fig. S10) and GR-CdS-15% (Co-Pi) composite have been performed. It is clear that the photocatalytic activity of GR-CdS-15% (Co-Pi) remains relatively stable in four continuous cycles (Fig. 3e). The inductively coupled plasmaoptical emission spectroscopy (ICP-OES) instrument analysis results about the reaction solution of GR-CdS-15% (Co-Pi) composite indicate that there is no significant leaching of the ions Cd<sup>2+</sup> and Co<sup>3+/2+</sup> after photocatalytic reaction (Table S3). The leakage of Cd<sup>2+</sup> is 0.02 ppm, while the leakage of Co<sup>3+/2+</sup> is almost negligible. But for the blank CdS NPs, the relative content of Cd<sup>2+</sup> leakage increases to 6.67 ppm under 5 h light irradiation. In addition, the XRD spectrum of used GR-CdS-15% (Co-Pi) composite shows negligible change compared with the fresh one as displayed in Fig. S11, which proves the structural stability of the materials. In general, the above results evidently confirm the outstanding photostability of GR-CdS-15% (Co-Pi) composites.

### 3.4. Mechanistic insights of photoredox-catalyzed reaction for cooperative 4-MTP conversion and H<sub>2</sub> generation

The complementary photo- and electrochemical measurements have been carried out to unveil the synergistic effect of GR and Co-Pi on increasing photocatalytic performance of CdS NPs, which are relevant with the separation and transfer efficiency of photogenerated carriers [17,54]. As sketched in Fig. 4a, transitory photocurrent-time plots of CdS NPs, GR-CdS and GR-CdS-(Co-Pi) composites are achieved through periodically turning on and off the illumination of light. Blank CdS NPs display the weakest photocurrent intensity, indicating the photoinduced charge carriers recombine severely [55]. The photocurrent density of binary GR-CdS is enhanced after the introduction of GR NSs, and the subsequent assembly of Co-Pi onto GR-CdS demonstrates the highest photocurrent intensity. To shed light on the charge transfer at the contact interface between photocatalyst and electrolyte, the electrochemical impedance spectroscopy (EIS) has also been carried out (Fig. 4b) [56]. At high frequency, the EIS curve of GR-CdS-(Co-Pi) shows the smallest arc of the three catalysts, manifesting that a smaller resistance and a more effective charge migration between GR-CdS-(Co-Pi) and electrolyte are obtained than those of GR-CdS and blank CdS NPs [52,53]. Photoluminescence (PL) measurement is carried out to further investigate the behavior of photoinduced charge carriers. As displayed in Fig. 4c, the PL emission intensity of GR-CdS-(Co-Pi) decreases

obviously at 370 nm excitation, indicating that the recombination of photoinduced charges can be effectively hindered after decorating GR and Co-Pi. The noticeable enhancement of the photoredox-catalyzed performance and photostability of the GR-CdS-(Co-Pi) composite is attributed to the synergy of dual cocatalysts. In such dual-cocatalyst system, the GR NSs can effectively transport and accept photoinduced electrons, while the Co-Pi as hole transfer relay station can rapidly transfer photoexcited holes to prevent CdS NPs from suffering photo-corrosion [32,34].

For the sake of revealing the potential reaction mechanism of the photoredox-catalyzed dehydrocoupling of 4-MTP over GR-CdS-(Co-Pi), a series of control experiments under different reaction conditions are carried out. As disclosed in Fig. 4d, upon removal of catalyst or light irradiation, no products are detected, suggesting that the reaction is a light-driven catalytic process [57]. Adding CCl<sub>4</sub> into the system as the electron scavenger retards the H<sub>2</sub> evolution, whereas the formation of 4-MPD ceases after adding hole scavenger triethanolamine (TEOA), suggesting that photoexcited electrons and holes respectively participate in the formation of H<sub>2</sub> and 4-MPD [23,58]. Furthermore, the presence of 5, 5-dimethyl-1-pyrrolin-N-oxide (DMPO) also significantly inhibits the 4-MPD production, indicating that the formation of 4-MPD proceeds *via* radical intermediates [59].

In order to further identify the radical intermediates formed *in situ* on CdS, GR-CdS and GR-CdS-(Co-Pi), the electron paramagnetic resonance (EPR) spectroscopy experiment with dimethylpyridine nitrogen oxide (DMPO) as the trapping agent has been attempted. As exhibited in Fig. 4e and f, the photocatalysts display six characteristic signal peaks indexed to the sulfur-centered radical (•SC<sub>6</sub>H<sub>4</sub>(OCH<sub>3</sub>)) intermediates ( $\alpha_N = 13.10$  and  $\alpha_H = 14.56$ , related to the nitrogen hyperfine splitting and hydrogen hyperfine splitting of the nitroxide nitrogen) under light illumination [60]. It is worth mentioning that the signal peaks intensity of sulfur-centered radicals of the GR-CdS-(Co-Pi) composite is strongest among all the samples, expressing that ternary composite facilitates the formation of reactive •SC<sub>6</sub>H<sub>4</sub>(OCH<sub>3</sub>) radicals, therefore further improving the photocatalytic performance [59]. Cyclic voltammetry (CV) measurements are carried out to figure out the effect of Co-Pi modification for thiols oxidation. As shown in Fig. S12, the oxidation potential of 4-MTP is measured to + 0.55 V vs. Ag/AgCl, which can be converted into + 0.75 V vs. NHE on the basis of the equation of E<sub>NHE</sub> = E<sub>Ag/AgCl</sub> + 0.20 V. The CV of GR-CdS-(Co-Pi) displays two couples of

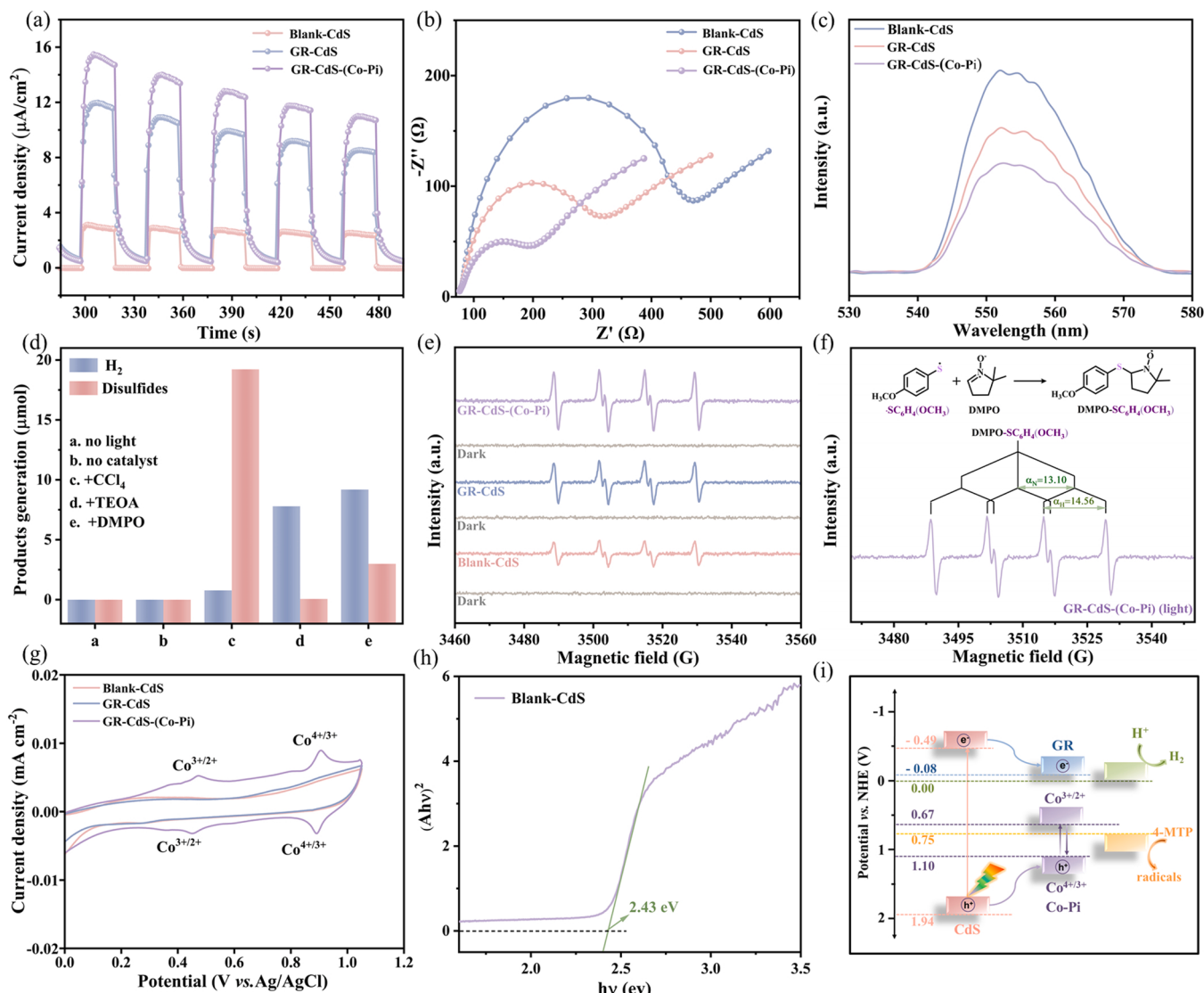


**Fig. 4.** (a) Transient photocurrent spectra. (b) EIS Nyquist curves. (c) PL plots with an excitation wavelength of 370 nm. (d) Control experiments for photocatalytic conversion of 4-MTP over GR-CdS-(Co-Pi) (The typical reaction conditions are as follows: 5 mg of photocatalyst, 50  $\mu$ mol of 4-MTP, 5 mL of MeCN, Ar atmosphere, 0.2 mmol of quenchers, full spectrum, 5 h). (e) EPR spectra of blank CdS, GR-CdS and GR-CdS-(Co-Pi) suspensions in MeCN solution containing 50  $\mu$ mol 4-MTP and 0.2 mmol DMPO with or without light irradiation for 5 min under argon atmosphere. (f) The quantitative analysis result of EPR spectrum of GR-CdS-(Co-Pi) composite with light irradiation. (g) CV plots of samples in electrolytes containing 0.2 mmol TBABF<sub>4</sub> in MeCN solution. (h) Tauc plot for optical band gap of blank CdS. (i) Schematic diagram of selective thiol oxidation into disulfide integrated with H<sub>2</sub> evolution.

reversible redox peaks at + 0.47 V vs. Ag/AgCl and + 0.90 V vs. Ag/AgCl (Fig. 4g), which are allocated to the redox couple of Co<sup>3+/2+</sup> and Co<sup>4+/3+</sup>, respectively [61]. The optical band gap of CdS is calculated to be 2.43 eV, which is obtained from the Tauc plot of the transformed Kubelka-Munk function (Fig. 4h) [54]. In the light of the Mott-Schottky curves (Fig. S13), CdS shows the trend of n-type semiconductor, and its flat band potential is fixed in - 0.69 V vs. Ag/AgCl. And the CB position of CdS is estimated at - 0.49 V vs. NHE based on the fact that the conduction band (CB) position of n-type semiconductor is closer to its flat band potential. Taking into account the band gap data obtained previously, the valence band (VB) position of CdS is calculated to be 1.94 V based on the formula of  $E_{VB} = E_{CB} + E_g$  ( $E_{VB}$ ,  $E_{CB}$ , and  $E_g$  respectively are the energy values of VB, CB, and band gap). It has been reported that the calculated Fermi level ( $E_F$ ) of GR is ca. - 0.08 V vs. NHE [62]. As displayed in Fig. 4i, it can be inferred that the photoexcited holes with sufficient thermodynamic driving force can facilely oxidize Co<sup>3+/2+</sup> of CoPi to Co<sup>4+/3+</sup>, and Co<sup>4+/3+</sup> then oxidizes 4-MTP to 4-MPD and returns to Co<sup>3+/2+</sup> [63,64], and the photogenerated electrons from CdS can

transfer to the GR NSs, thereby enhancing the lifetime and migration of electron-hole pairs and providing active sites for the proton reduction to H<sub>2</sub>.

In light of the aforementioned discussion, a feasible mechanism of dehydrocoupling of 4-MTP to 4-MPD over GR-CdS-(Co-Pi) is proposed as the following. As manifested in Fig. 5, under the irradiation of UV-vis light, electrons are photoexcited from the VB of CdS NPs to the CB, leaving holes in the VB contemporaneously. The decorated Co-Pi supports the efficient separation of photogenerated electron and hole pairs by cyclically capturing photoinduced holes [65–67]. Subsequently, the holes trapped by Co-Pi oxidize the Co ions to higher oxidation state, which further activate and split the S-H bond of 4-MTP to produce  $\bullet$ SC<sub>6</sub>H<sub>4</sub>(OCH<sub>3</sub>) radicals and protons, and then returns to its initial oxidation state. Then, these sulfur-centered radicals couple with each other to form 4-MPD. Meanwhile, owing to the addition of GR NSs as electron conductive platforms and active sites, the photoexcited electrons can facilely migrate to GR NSs and then directly combine with surface-adsorbed protons for finally catalytic H<sub>2</sub> formation [68].

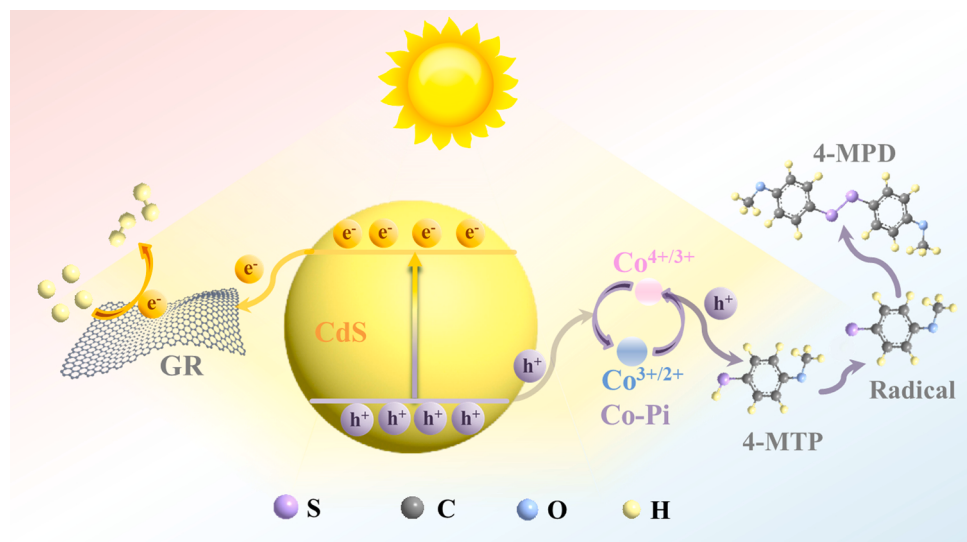


**Fig. 5.** Proposed reaction mechanism of photoredox-catalyzed coupling reaction for 4-MTP conversion and  $H_2$  generation over GR-CdS-(Co-Pi) under light irradiation.

Consequently, the synergistic effect of GR and Co-Pi dual cocatalysts for electron capture and hole consumption ensures the efficient separation of photoinduced charge carriers, thus evidently ameliorating the photoredox-catalyzed activity and anti-photocorrosion capacity of GR-CdS-(Co-Pi) composite.

#### 4. Conclusions

To sum up, a ternary reduced graphene oxide (GR)-CdS-cobalt phosphate (Co-Pi) composite with low-cost and efficient dual cocatalysts has been successfully constructed for efficient photocatalytic splitting of thiols to disulfides and  $H_2$  under mild condition. Mechanism study suggests that the Co-Pi plays a vital role to accelerate the photo-generated holes output from CdS, while GR not only facilitates the transfer of photogenerated electrons but also provides active sites for  $H_2$  generation. Moreover, sulfur-centered radicals have been confirmed as the vital reactive intermediates during this photoredox-catalyzed process. Our methodology is compatible with various thiophenols, affording the corresponding disulfides with excellent selectivity. This work could shed new light of decorating earth-abundant dual-cocatalysts onto semiconductor photocatalysts to provide a cooperative coupling photoredox catalysis by coinstantaneous use of photoexcited electrons and holes toward efficient solar energy driven coproduction of  $H_2$  fuel and valuable fine chemicals.

#### CRediT authorship contribution statement

**Ming-Hui Sun:** Investigation, Validation, Writing – original draft, Formal analysis, Writing – review & editing. **Ming-Yu Qi:** Writing – review & editing, Formal analysis. **Zi-Rong Tang:** Funding acquisition, Resources, Project administration, Writing – review & editing. **Yi-Jun Xu:** Funding acquisition, Conceptualization, Resources, Project administration, Writing – review & editing, Supervision.

#### Declaration of Competing Interest

The authors declare that they have no known competing financial interests or personal relationships that could have appeared to influence the work reported in this paper.

#### Data Availability

Data will be made available on request.

#### Acknowledgements

This work was supported by the Natural Science Foundation of China (22172030, 22072023, 21872029, U1463204 and 21173045), the Program for National Science and Technology Innovation Leading Talents (00387072), the Program for Leading Talents of Fujian Universities, the 1st Program of Fujian Province for Top Creative Young Talents, and the Natural Science Foundation of Fujian Province (2017J07002 and 2019J01631).

#### Appendix A. Supporting information

Supplementary data associated with this article can be found in the online version at [doi:10.1016/j.apcatb.2022.122019](https://doi.org/10.1016/j.apcatb.2022.122019).

#### References

- [1] J.-H. Ryu, R.T. Chacko, S. Jiwpanich, S. Bickerton, R.P. Babu, S. Thayumanavan, Self-cross-linked polymer nanogels: a versatile nanoscopic drug delivery platform, *J. Am. Chem. Soc.* 132 (2010) 17227–17235, <https://doi.org/10.1021/ja1069932>.
- [2] A.M. Almeida, R. Li, S.H. Gellman, Parallel beta-sheet secondary structure is stabilized and terminated by interstrand disulfide cross-linking, *J. Am. Chem. Soc.* 134 (2012) 75–78, <https://doi.org/10.1021/ja208856c>.
- [3] L. Li, Z. Li, A. Yoshimura, C. Sun, T. Wang, Y. Chen, Z. Chen, A. Littlejohn, Y. Xiang, P. Hundekar, S.F. Bartolucci, J. Shi, S.-F. Shi, V. Meunier, G.-C. Wang, N. Koratkar, Vanadium disulfide flakes with nanolayered titanium disulfide coating as cathode materials in lithium-ion batteries, *Nat. Commun.* 10 (2019) 1764, <https://doi.org/10.1038/s41467-019-10940-w>.
- [4] D. Fass, C. Thorpe, Chemistry and enzymology of disulfide cross-linking in proteins, *Chem. Rev.* 118 (2018) 293–322, <https://doi.org/10.1021/acs.chemrev.7b00123>.
- [5] F. Hosseinpour, H. Golchoubian, Mild and highly efficient transformation of thiols to symmetrical disulfides using urea-hydrogen peroxide catalyzed by a Mn(III)-salen complex, *Catal. Lett.* 111 (2006) 165–168, <https://doi.org/10.1007/s10562-006-0141-8>.
- [6] B. Zeynizadeh, N. Iranpoor, Oxidative coupling of thiols to disulfides with Ti(IV) in the presence of NaI under air atmosphere, *J. Chin. Chem. Soc.* 50 (2003) 849–852, <https://doi.org/10.1002/jccs.200300118>.
- [7] M. Oba, K. Tanaka, K. Nishiyama, W. Ando, Aerobic oxidation of thiols to disulfides catalyzed by diaryl tellurides under photosensitized conditions, *J. Org. Chem.* 76 (2011) 4173–4177, <https://doi.org/10.1021/jo200496r>.
- [8] M.-Y. Qi, M. Conte, M. Anpo, Z.-R. Tang, Y.-J. Xu, Cooperative coupling of oxidative organic synthesis and hydrogen production over semiconductor-based photocatalysts, *Chem. Rev.* 121 (2021) 13051–13085, <https://doi.org/10.1021/acs.chemrev.1c00197>.

[9] L. Xu, X. Deng, Z. Li, Photocatalytic splitting of thiols to produce disulfides and hydrogen over Pt5/ZnIn2S4 nanocomposites under visible light, *Appl. Catal., B* 234 (2018) 50–55, <https://doi.org/10.1016/j.apcatb.2018.04.030>.

[10] J.B. Arterburn, M.C. Perry, S.L. Nelson, B.R. Dible, M.S. Holguin, Rhenium-catalyzed oxidation of thiols and disulfides with sulfoxides, *J. Am. Chem. Soc.* 119 (1997) 9309–9310, <https://doi.org/10.1021/ja972013r>.

[11] A. Corma, T. Rodenas, M.J. Sabater, Aerobic oxidation of thiols to disulfides by heterogeneous gold catalysts, *Chem. Sci.* 3 (2012) 398–404, <https://doi.org/10.1039/C1SC00466B>.

[12] T. Kondo, T. Mitsudo, Metal-catalyzed carbon-sulfur bond formation, *Chem. Rev.* 100 (2000) 3205–3220, <https://doi.org/10.1021/cr9902749>.

[13] H.J. Kim, J.H. Yoon, S. Yoon, Photooxidative coupling of thiophenol derivatives to disulfides, *J. Phys. Chem. A* 114 (2010) 12010–12015, <https://doi.org/10.1021/jp1077483>.

[14] H. Xu, Y.-F. Zhang, X. Lang, TEMPO visible light photocatalysis: the selective aerobic oxidation of thiols to disulfides, *Chin. Chem. Lett.* 31 (2020) 1520–1524, <https://doi.org/10.1016/j.cclet.2019.10.024>.

[15] D.R. Dreyer, H.-P. Jia, A.D. Todd, J. Geng, C.W. Bielawski, Graphite oxide: a selective and highly efficient oxidant of thiols and sulfides, *Org. Biomol. Chem.* 9 (2011) 7292–7295, <https://doi.org/10.1039/C1OB06102J>.

[16] L. Cheng, Q.J. Xiang, Y.L. Liao, H.W. Zhang, CdS-based photocatalysts, *Energy Environ. Sci.* 11 (2018) 1362–1391, <https://doi.org/10.1039/C7EE03640J>.

[17] Y.-H. Li, F. Zhang, Y. Chen, J.-Y. Li, Y.-J. Xu, Photoredox-catalyzed biomass intermediate conversion integrated with H<sub>2</sub> production over Ti<sub>3</sub>C<sub>2</sub>T<sub>x</sub>/CdS composites, *Green Chem.* 22 (2020) 163–169, <https://doi.org/10.1039/C9GC03332G>.

[18] M. Darwish, A. Mohammadi, N. Assi, Integration of nickel doping with loading on graphene for enhanced adsorptive and catalytic properties of CdS nanoparticles towards visible light degradation of some antibiotics, *J. Hazard. Mater.* 320 (2016) 304–314, <https://doi.org/10.1016/j.jhazmat.2016.08.043>.

[19] P. Zhang, D.Y. Luan, X.W. Lou, Fabrication of CdS frame-in-cage particles for efficient photocatalytic hydrogen generation under visible-light irradiation, *Adv. Mater.* 32 (2020), 2004561, <https://doi.org/10.1002/adma.202004561>.

[20] Q. Li, B. Guo, J. Yu, J. Ran, B. Zhang, H. Yan, J.R. Gong, Highly efficient visible-light-driven photocatalytic hydrogen production of CdS-cluster-decorated graphene nanosheets, *J. Am. Chem. Soc.* 133 (2011) 10878–10884, <https://doi.org/10.1021/ja2025454>.

[21] Y.-L. Wu, M.-Y. Qi, C.-L. Tan, Z.-R. Tang, Y.-J. Xu, Photocatalytic selective oxidation of aromatic alcohols coupled with hydrogen evolution over CdS/WO<sub>3</sub> composites, *Chin. J. Catal.* 43 (2022) 1851–1859, [https://doi.org/10.1016/S1872-2067\(21\)63989-X](https://doi.org/10.1016/S1872-2067(21)63989-X).

[22] J. Yang, D. Wang, H. Han, C. Li, Roles of cocatalysts in photocatalysis and photoelectrocatalysis, *Acc. Chem. Res.* 46 (2013) 1900–1909, <https://doi.org/10.1021/ar300227e>.

[23] M.-Y. Qi, Y.-H. Li, F. Zhang, Z.-R. Tang, Y. Xiong, Y.-J. Xu, Switching light for site-directed spatial loading of cocatalysts onto heterojunction photocatalysts with boosted redox catalysis, *ACS Catal.* 10 (2020) 3194–3202, <https://doi.org/10.1021/acscatal.9b05420>.

[24] Q. Li, X. Li, S. Wageh, A.A. Al-Ghamdi, J. Yu, CdS/graphene nanocomposite photocatalysts, *Adv. Energy Mater.* 5 (2015), 1500010, <https://doi.org/10.1002/aenm.201500010>.

[25] X.-z Li, B. Weng, N. Zhang, Y.-J. Xu, In situ synthesis of hierarchical In<sub>2</sub>S<sub>3</sub>-graphene nanocomposite photocatalyst for selective oxidation, *RSC Adv.* 4 (2014) 64484–64493, <https://doi.org/10.1039/C4RA13764G>.

[26] S. Liu, B. Weng, Z.-R. Tang, Y.-J. Xu, Constructing one-dimensional silver nanowire-doped reduced graphene oxide integrated with CdS nanowire network hybrid structures toward artificial photosynthesis, *Nanoscale* 7 (2015) 861–866, <https://doi.org/10.1039/C4NR04229H>.

[27] Q. Quan, X. Lin, N. Zhang, Y.-J. Xu, Graphene and its derivatives as versatile templates for materials synthesis and functional applications, *Nanoscale* 9 (2017) 2398–2416, <https://doi.org/10.1039/C6NR09439B>.

[28] B. Weng, J. Wu, N. Zhang, Y.-J. Xu, Observing the role of graphene in boosting the two-electron reduction of oxygen in graphene-WO<sub>3</sub> nanorod photocatalysts, *Langmuir* 30 (2014) 5574–5584, <https://doi.org/10.1021/la4048566>.

[29] J.R. Prekodravac, D.P. Kepić, J.C. Colmenares, D.A. Giannakoudakis, S. P. Jovanović, A comprehensive review on selected graphene synthesis methods: from electrochemical exfoliation through rapid thermal annealing towards biomass pyrolysis, *J. Mater. Chem. C* 9 (2021) 6722–6748, <https://doi.org/10.1039/DTC01316E>.

[30] Y. Wang, Y. Wang, R. Jiang, R. Xu, Cobalt phosphate-ZnO composite photocatalysts for oxygen evolution from photocatalytic water oxidation, *Ind. Eng. Chem. Res.* 51 (2012) 9945–9951, <https://doi.org/10.1021/ie2027469>.

[31] P. Kuang, L. Zhang, B. Cheng, J. Yu, Enhanced charge transfer kinetics of Fe<sub>2</sub>O<sub>3</sub>/CdS composite nanorod arrays using cobalt-phosphate as cocatalyst, *Appl. Catal., B* 218 (2017) 570–580, <https://doi.org/10.1016/j.apcatb.2017.07.002>.

[32] K.-Q. Lu, M.-Y. Qi, Z.-R. Tang, Y.-J. Xu, Earth-abundant MoS<sub>2</sub> and cobalt phosphate dual cocatalysts on 1D CdS nanowires for boosting photocatalytic hydrogen production, *Langmuir* 35 (2019) 11056–11065, <https://doi.org/10.1021/acs.langmuir.9b01409>.

[33] X. Li, J. Wan, Y. Ma, Y. Wang, X. Li, Study on cobalt-phosphate (Co-Pi) modified BiVO<sub>4</sub>/Cu<sub>2</sub>O photoanode to significantly inhibit photochemical corrosion and improve the photoelectrochemical performance, *Chem. Eng. J.* 404 (2021) 127054, <https://doi.org/10.1016/j.cej.2020.127054>.

[34] K.-Q. Lu, Y.-H. Li, F. Zhang, M.-Y. Qi, X. Chen, Z.-R. Tang, Y.M.A. Yamada, M. Anpo, M. Conte, Y.-J. Xu, Rationally designed transition metal hydroxide nanosheet arrays on graphene for artificial CO<sub>2</sub> reduction, *Nat. Commun.* 11 (2020) 5181, <https://doi.org/10.1038/s41467-020-18944-1>.

[35] N. Zhang, Y.-H. Zhang, X.-Y. Pan, X.-Z. Fu, S.-Q. Liu, Y.-J. Xu, Assembly of CdS nanoparticles on the two-dimensional graphene scaffold as visible-light-driven photocatalyst for selective organic transformation under ambient conditions, *J. Phys. Chem. C* 115 (2011) 23501–23511, <https://doi.org/10.1021/jp208661n>.

[36] Q. Lin, Y.-H. Li, M.-Y. Qi, J.-Y. Li, Z.-R. Tang, M. Anpo, Y.M.A. Yamada, Y.-J. Xu, Photoredox dual reaction for selective alcohol oxidation and hydrogen evolution over nickel surface-modified ZnIn<sub>2</sub>S<sub>4</sub>, *Appl. Catal. B* 271 (2020), 118946, <https://doi.org/10.1016/j.apcatb.2020.118946>.

[37] M.-Y. Qi, Y.-H. Li, M. Anpo, Z.-R. Tang, Y.-J. Xu, Efficient photoredox-mediated C–C coupling organic synthesis and hydrogen production over engineered semiconductor quantum dots, *ACS Catal.* 10 (2020) 14327–14335, <https://doi.org/10.1021/acscatal.0c04237>.

[38] M.-Q. Yang, Y. Zhang, N. Zhang, Z.-R. Tang, Y.-J. Xu, Visible-light-driven oxidation of primary C–H bonds over CdS with dual co-catalysts graphene and TiO<sub>2</sub>, *Sci. Rep.* 3 (2013) 3314, <https://doi.org/10.1038/srep03314>.

[39] Y. Surendranath, M.W. Kanan, D.G. Nocera, Mechanistic studies of the oxygen evolution reaction by a cobalt–phosphate catalyst at neutral pH, *J. Am. Chem. Soc.* 132 (2010) 16501–16509, <https://doi.org/10.1021/ja106102b>.

[40] K.J. McDonald, K.-S. Choi, Photodeposition of Co-based oxygen evolution catalysts on alpha-Fe<sub>2</sub>O<sub>3</sub> photoanodes, *Chem. Mater.* 23 (2011) 1686–1693, <https://doi.org/10.1021/cm1020614>.

[41] N. Zhang, M.-Q. Yang, Z.-R. Tang, Y.-J. Xu, CdS–graphene nanocomposites as visible light photocatalyst for redox reactions in water: a green route for selective transformation and environmental remediation, *J. Catal.* 303 (2013) 60–69, <https://doi.org/10.1016/j.jcat.2013.02.026>.

[42] M.-Q. Yang, C. Han, Y.-J. Xu, Insight into the effect of highly dispersed MoS<sub>2</sub> versus layer-structured MoS<sub>2</sub> on the photocorrosion and photoactivity of CdS in graphene-CdS-MoS<sub>2</sub> composition, *J. Phys. Chem. C* 119 (2015) 27234–27246, <https://doi.org/10.1021/acs.jpcc.5b08016>.

[43] L. Ge, C. Han, X. Xiao, L. Guo, In situ synthesis of cobalt–phosphate (Co–Pi) modified g-C<sub>3</sub>N<sub>4</sub> photocatalysts with enhanced photocatalytic activities, *Appl. Catal. B* 142 (2013) 414–422, <https://doi.org/10.1016/j.apcatb.2013.05.051>.

[44] P. Wang, S. Xu, Y. Xia, X. Wang, H. Yu, J. Yu, Synergistic effect of CoPi-hole and Cu (II)-electron cocatalysts for enhanced photocatalytic activity and photoinduced stability of Ag<sub>3</sub>PO<sub>4</sub>, *Phys. Chem. Chem. Phys.* 19 (2017) 10309–10316, <https://doi.org/10.1039/C7CP01043E>.

[45] Z.B. Yu, Y.P. Xie, G. Liu, G.Q. Lu, X.L. Ma, H.-M. Cheng, Self-assembled CdS/Au/ZnO heterostructure induced by surface polar charges for efficient photocatalytic hydrogen evolution, *J. Mater. Chem. A* 1 (2013) 2773–2776, <https://doi.org/10.1039/C3TA01476B>.

[46] L.J. Zhang, S. Li, B.K. Liu, D.J. Wang, T.F. Xie, Highly efficient CdS/WO<sub>3</sub> photocatalysts: Z-Scheme photocatalytic mechanism for their enhanced photocatalytic H<sub>2</sub> evolution under visible light, *ACS Catal.* 4 (2014) 3724–3729, <https://doi.org/10.1021/acscsm.4c500794j>.

[47] M.F. Shao, F.Y. Ning, M. Wei, D.G. Evans, X. Duan, Hierarchical nanowire arrays based on ZnO core-layered double hydroxide shell for largely enhanced photoelectrochemical water splitting, *Adv. Funct. Mater.* 24 (2014) 580–586, <https://doi.org/10.1002/adfm.201301889>.

[48] G.J. Ai, R. Mo, H.X. Li, J.X. Zhong, Cobalt phosphate modified TiO<sub>2</sub> nanowire arrays as co-catalysts for solar water splitting, *Nanoscale* 7 (2015) 6722–6728, <https://doi.org/10.1039/C5NR00863H>.

[49] T. Di, B. Zhu, J. Zhang, B. Cheng, J. Yu, Enhanced photocatalytic H<sub>2</sub> production on CdS nanorod using cobalt–phosphate as oxidation cocatalyst, *Appl. Surf. Sci.* 389 (2016) 775–782, <https://doi.org/10.1016/j.apsusc.2016.08.002>.

[50] B. Cao, Y. Jiang, C. Wang, W. Wang, L. Wang, M. Niu, W. Zhang, Y. Li, S.-T. Lee, Synthesis and lasing properties of highly ordered CdS nanowire arrays, *Adv. Funct. Mater.* 17 (2007) 1501–1506, <https://doi.org/10.1002/adfm.200601179>.

[51] V. Nagyte, D.J. Kelly, A. Felten, G. Picardi, Y. Shin, A. Alieva, R.E. Worsley, K. Parvez, S. Dehm, R. Krupke, S.J. Haigh, A. Oikonomou, A.J. Pollard, C. Casiraghi, Raman fingerprints of graphene produced by anodic electrochemical exfoliation, *Nano Lett.* 20 (2020) 3411–3419, <https://doi.org/10.1021/acs.nanolett.0c00332>.

[52] C. Han, Z. Chen, N. Zhang, J.C. Colmenares, Y.-J. Xu, Hierarchically CdS decorated 1D ZnO nanorods-2D graphene hybrids: low temperature synthesis and enhanced photocatalytic performance, *Adv. Funct. Mater.* 25 (2015) 221–229, <https://doi.org/10.1002/adfm.201402443>.

[53] N. Zhang, M.-Q. Yang, Z.-R. Tang, Y.-J. Xu, Toward improving the graphene–semiconductor composite photoactivity via the addition of metal ions as generic interfacial mediator, *ACS Nano* 8 (2014) 623–633, <https://doi.org/10.1021/nn405242t>.

[54] C.-L. Tan, M.-Y. Qi, Z.-R. Tang, Y.-J. Xu, Cocatalyst decorated ZnIn<sub>2</sub>S<sub>4</sub> composites for cooperative alcohol conversion and H<sub>2</sub> evolution, *Appl. Catal. B* 298 (2021), 120541, <https://doi.org/10.1016/j.apcatb.2021.120541>.

[55] H. Yang, Z. Jin, D. Liu, K. Fan, G. Wang, Visible light harvesting and spatial charge separation over the creative Ni/CdS/Co<sub>3</sub>O<sub>4</sub> photocatalyst, *J. Phys. Chem. C* 122 (2018) 10430–10441, <https://doi.org/10.1021/acs.jpcc.8b01666>.

[56] Y.-S. Xie, L. Yuan, N. Zhang, Y.-J. Xu, Light-tuned switching of charge transfer channel for simultaneously boosted photoactivity and stability, *Appl. Catal. B* 238 (2018) 19–26, <https://doi.org/10.1016/j.apcatb.2018.07.006>.

[57] J.-Y. Li, L. Yuan, S.-H. Li, Z.-R. Tang, Y.-J. Xu, One-dimensional copper-based heterostructures toward photo-driven reduction of CO<sub>2</sub> to sustainable fuels and feedstocks, *J. Mater. Chem. A* 7 (2019) 8676–8689, <https://doi.org/10.1039/C8TA12427B>.

[58] J.-Y. Li, Y.-H. Li, F. Zhang, Z.-R. Tang, Y.-J. Xu, Visible-light-driven integrated organic synthesis and hydrogen evolution over 1D/2D CdS-Ti<sub>3</sub>C<sub>2</sub>T<sub>x</sub> MXene composites, *Appl. Catal. B* 269 (2020), 118783, <https://doi.org/10.1016/j.apcatb.2020.118783>.

[59] C. Huang, R.-N. Ci, J. Qiao, X.-Z. Wang, K. Feng, B. Chen, C.-H. Tung, L.-Z. Wu, Direct allylic C(sp<sup>3</sup>)-H and vinylic C(sp<sup>2</sup>)-H thiolation with hydrogen evolution by quantum dots and visible light, *Angew. Chem. Int. Ed.* 60 (2021) 11779–11783, <https://doi.org/10.1002/anie.202101947>.

[60] M. Jiang, H. Li, H. Yang, H. Fu, Room-temperature arylation of thiols: breakthrough with aryl chlorides, *Angew. Chem. Int. Ed.* 56 (2017) 874–879, <https://doi.org/10.1002/anie.201610414>.

[61] J. Wang, M.Y. Qi, X.X. Wang, W.Y. Su, Cooperative hydrogen production and C-C coupling organic synthesis in one photoredox cycle, *Appl. Catal. B* 302 (2022) 120812, <https://doi.org/10.1016/j.apcatb.2021.120812>.

[62] Y.-H. Zhang, Z. Chen, S.-Q. Liu, Y.-J. Xu, Size effect induced activity enhancement and anti-photocorrosion of reduced graphene oxide/ZnO composites for degradation of organic dyes and reduction of Cr(VI) in water, *Appl. Catal. B* 140–141 (2013) 598–607, <https://doi.org/10.1016/j.apcatb.2013.04.059>.

[63] B. Pan, Y. Zhou, W. Su, X. Wang, Enhanced photocatalytic CO<sub>2</sub> conversion over LaPO<sub>4</sub> by introduction of CoCl<sub>2</sub> as a hole mediator, *RSC Adv.* 6 (2016) 34744–34747, <https://doi.org/10.1039/C6RA02958B>.

[64] G.-H. Moon, M. Yu, C.K. Chan, H. Tueysuez, Highly active cobalt-based electrocatalysts with facile incorporation of dopants for the oxygen evolution reaction, *Angew. Chem. Int. Ed.* 58 (2019) 3491–3495, <https://doi.org/10.1002/anie.201813052>.

[65] R.J. Pleus, H. Waden, W. Saak, D. Haase, S. Pohl, Preparation of the first sulfur-containing cobalt and nickel complexes stabilised by the macrocyclic cyclam ligand; observation of S-H bond activation, *J. Chem. Soc. Dalton Trans.* (1999) 2601–2610, <https://doi.org/10.1039/A902015B>.

[66] A.M. Poitras, M.W. Bezpalko, B.M. Foxman, C.M. Thomas, Cooperative activation of O-H and S-H bonds across the Co-P bond of an N-heterocyclic phosphido complex, *Dalton Trans.* 48 (2019) 3074–3079, <https://doi.org/10.1039/C8DT05052J>.

[67] G. Ai, H. Li, S. Liu, R. Mo, J. Zhong, Solar water splitting by TiO<sub>2</sub>/CdS/Co-Pi nanowire array photoanode enhanced with Co-Pi as hole transfer relay and CdS as light absorber, *Adv. Funct. Mater.* 25 (2015) 5706–5713, <https://doi.org/10.1002/adfm.201502461>.

[68] N. Zhang, Y.-H. Zhang, M.-Q. Yang, Z.-R. Tang, Y.-J. Xu, A critical and benchmark comparison on graphene-, carbon nanotube-, and fullerene-semiconductor nanocomposites as visible light photocatalysts for selective oxidation, *J. Catal.* 299 (2013) 210–221, <https://doi.org/10.1016/j.jcat.2012.11.021>.